Geophysical Research Letters®

Key Points:

- We explore the hypothesis that the ongoing uplift in the Rhenish Massif is (partly) due to melt accumulating in the lithosphere
- Observed ground deformation would require the intrusion of up to ~0.045 km³/yr into one or more horizontal magma lenses
- We test different deformation sources and discuss the feasibility, limitations and possible interpretations of the resulting models

Correspondence to:

F. Silverii,
francesca.silverii@ingv.it

Author Contributions:

Conceptualization: E. Rivalta
Formal analysis: F. Silverii
Funding acquisition: E. Rivalta
Investigation: F. Silverii, L. Mantiloni, E. Rivalta, T. Dahm
Methodology: F. Silverii, L. Mantiloni
Supervision: E. Rivalta, T. Dahm
Validation: F. Silverii, L. Mantiloni
Visualization: F. Silverii
Writing – original draft: F. Silverii
Writing – review & editing: F. Silverii, L. Mantiloni, E. Rivalta, T. Dahm

Lithospheric Sill Intrusions and Present-Day Ground Deformation at Rhenish Massif, Central Europe

F. Silverii[1,2] , **L. Mantiloni[1,3]** , **E. Rivalta[1,4]** , and **T. Dahm[1,3]**

[1]Physics of Earthquakes and Volcanoes, German Research Centre for Geosciences (GFZ), Potsdam, Germany, [2]National Institute for Geophysics and Volcanology (INGV), Osservatorio Nazionale Terremoti, Rome, Italy, [3]Institute of Geosciences, University of Potsdam, Potsdam, Germany, [4]Department of Geophysics, University of Bologna, Bologna, Italy

Abstract The Rhenish Massif in Central Europe, which includes the Eifel Volcanic Fields, has shown ongoing ground deformation and signs of possible unrest. A buoyant plume exerting uplift forces at the bottom of the lithosphere was proposed to explain such deformation; the hypothesis of (possibly concurrent) melt accumulation in the crust/lithospheric mantle has not been explored yet. Here, we test deformation models in an elastic half-space considering sources of varying aspect ratio, size and depth. We explore the effects of data coverage, noise and uncertainty on the inferred source parameters. We find that the observed deformation would require melt accumulation in sub-horizontal sill-like structures expanding at the rate of up to ~0.045 km³/yr. We discuss feasibility, limitations and possible interpretations of our resulting models and elaborate on further observations which may help constrain the structure of the Rhenish Massif magmatic system.

Plain Language Summary Geodetic observations over the last 20 years recorded small but steady ground deformation over a wide area centered on the Eifel Volcanic Fields, Germany, where volcanism has occurred as recently as 11,000 years ago. Together with geophysical and geochemical evidences of possible ongoing unrest, the observed deformation has renewed interest over the origin of volcanism in the region. The deformation has been tentatively related to a buoyant plume in the asthenosphere. Here, we test whether the deformation may be, at least partially, originating in the lithosphere. We find that deformation data would be consistent with melt intrusions in one or more horizontal lenses located in the lithosphere, but limitations exist due to models simplifications. We discuss feasibility, limitations and possible interpretations of our results, and what additional data may improve our knowledge on the underlying magmatic system.

1. Introduction

The Rhenish Massif (RHM) is a large lithospheric block located in Central Europe (Figure 1a) embedding several volcanic fields, as Westerwald, Eifel, and Siebengebirge (e.g., Prodehl et al., 2006). These are part of the Central European Volcanic Fields (CEVF) which developed during the Tertiary, and partly the Quaternary, over a belt region spanning France, central Germany, Czech Republic, and south-west Poland (Schmincke, 2007). Activity at Eifel Volcanic Fields (EVF) started in the Tertiary with the Hocheifel volcanic field formation (Fekiacova et al., 2007). In the Quaternary two volcanic fields formed west and east of Hocheifel (West EVF and East EVF; green dots in Figure 1). The late Quaternary volcanism culminated in the Laacher See Volcano eruption in East EVF at 13 ka (volcanic explosivity index VEI = 6) and continued until ~11 ka (Förster et al., 2020; Nowell et al., 2006; Reinig et al., 2021; Schmincke, 2007). Paleo-deformation studies mostly based on fluvial incision showed that the RHM experienced several periods of uplift with variable rates in space and time (Demoulin & Hallot, 2009), up to 0.3 mm/yr starting from the Quaternary (Meyer & Stets, 2007).

The predominant physical mechanism behind CEVF intraplate magmatism, and in particular of RHM, is still debated. Based on geochemical and geophysical evidence (deep-mantle features of volcanic rocks and gases, low seismic velocity anomaly from ~50 to ~410 km depth), magmatism is often related to a mantle plume located underneath RHM (e.g., Ritter, 2007; Ritter et al., 2001; Walker et al., 2007). This hypothesis is, however, inconsistent with the lack of a clear space-time progression in the RHM volcanism pattern, which would suggest a hotspot track, and the volume of erupted magma is small compared to established intraplate hotspot volcanic regions as Iceland or Hawaii. Several geochemical, petrological, and geodynamic studies support alternative
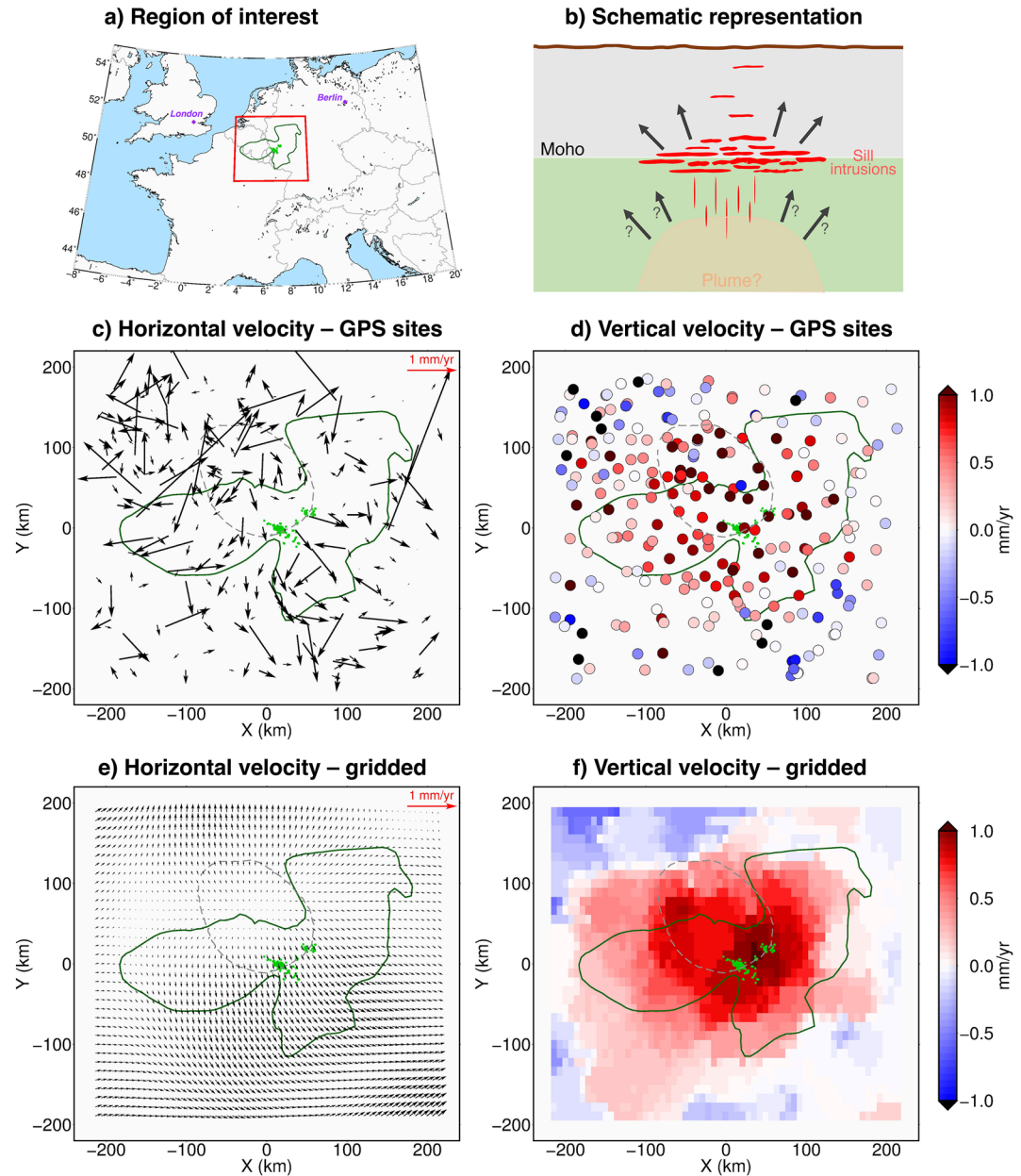
Figure 1. (a) Geographic location of the study region (red rectangle). Green dots are centers of Quaternary EVF activity, dark green line contours the Rhenish Massif and dashed gray contour outlines area of significant (>2σ) dilatation rate estimated from Kreemer et al. (2020). (b) Schematic representation of the possible deformation sources. (c to f) Velocity spatial distribution at GPS sites and grid nodes.

models linking the magmatism at RHM to plate tectonic processes associated with the Alpine collision (e.g., Jung et al., 2005; Lustrino & Carminati, 2007; Regenauer-Lieb, 1998; Wilson & Downes, 1992).

Debate over the source of volcanism, availability of new/reprocessed data and signs of possible ongoing unrest at EVF have renewed the interest about this area. Recent reappraisal of past seismic data sets (Dahm et al., 2020) and existing petrological and geophysical studies (Bräuer et al., 2013; Hensch et al., 2019) provided evidences of melt in lower crust/upper mantle. In particular, a long-range seismic refraction experiment in 1978–1979 (Mechie et al., 1983) showed a decrease in seismic compressional wave velocities (from 8.1 to 6.3 km/s) in the upper mantle, at the crust-mantle boundary (Moho), below the currently uplifting RHM. Dahm et al. (2020) interpreted this as a sub-horizontal, thin (~6 km), wide (~300 km) magma reservoir with a peak melt fraction of ~10%. Signs

of ongoing unrest involve degassing at mofettes and mineral springs (Bräuer et al., 2013; Caracausi et al., 2016), occurrence, since 2013, of deep low-frequency earthquakes in the lower crust and upper mantle beneath Laacher See Volcano (Hensch et al., 2019), and ongoing surface deformation (Henrion et al., 2020; Kreemer et al., 2020). Global Positioning System (GPS) data over the last ∼20 years show uplift in RHM area with peak rates >1 mm/yr and lower horizontal velocities with heterogeneous directions, but revealing areal dilatation approximately coincident with the uplifting area. This deformation was interpreted by Kreemer et al. (2020) as the effect of a buoyant plume impinging the lithosphere, modeled through a distribution of half-space vertical forces exerted on a plane at ∼50 km depth.

Given the evidences of melt accumulation at the Moho and at shallower depths, in the brittle crust, that would presumably cause some deformation at the surface, it appears important to explore the hypothesis that the observed deformation originates in full or partly within the lithosphere (Figure 1b), which is estimated to be rather thin (60 − 100 km) across the CEVF (Artemieva, 2019). Here we tested this using the GPS long-term linear trends (velocities) estimated by Kreemer et al. (2020), exploring different source solutions, shapes and depths in an elastic half-space and analyzing the effect of different data coverage, noise and uncertainty. This is nonetheless challenging due to the regional scale of the observed deformation and its overall small rates. We discuss the feasibility, limitations and possible interpretations of the resulting models.

2. Data

Kreemer et al. (2020) computed velocities from position time-series between January 2000 and October 2019, both at available GPS sites and as gridded values (at 0.1° steps, i.e., ∼10 km) obtained after data post-processing. This involves steps of despeckling velocities computed at GPS sites (i.e., leveling out velocity values against outliers) and subsequent gridding. The vertical gridded component was further corrected for the effect of glacial isostatic adjustment (GIA), as modeled by Husson et al. (2018). The GPS horizontal velocities were used to compute strain-rate distribution, from which gridded horizontal velocities have been modeled. We used both data sets (at GPS sites and as gridded values) since they represent two end-members: velocities at GPS sites, free of possible artifacts but scattered and noisy, and post-processed gridded values, more uniform and with higher spatial resolution.

We focused on an area of about 400 km × 400 km (3.5°–9.5°E, 48.5°–51.9°N) that embeds the uplift region around the RHM (Figure 1) comprising 250 GPS sites and 2135 grid nodes. We projected the GPS sites/gridded longitude, latitude coordinates into a local metric Cartesian reference frame (X along west-east, Y along south-north) referred to the center of the study area (6.5°E, 50.2°N).

Since GIA was not previously removed from the provided vertical velocities at GPS sites, we derived the GIA correction from the difference between the provided corrected and non-corrected gridded velocities and removed it from the vertical GPS velocities (Figure S1 in Supporting Information S1). The vertical data show a spatially coherent uplift area over the Rhenish Massif region with highest values (∼1–3 mm/yr) at EVF (Figures 1d and 1f), while subsidence is probably related to noise and/or residual trends at continental scale (Kreemer et al., 2020).

In general, the horizontal velocities are lower than the vertical ones (∼0.33 mm/yr of maximum horizontal separation rate across the uplift anomaly) and show a less clear pattern (Figure 1c). However, they reveal an extension region slightly offset north-west from the highest uplift area (Kreemer et al., 2020) (gray line in Figure 1; Figure S2 in Supporting Information S1).

GPS velocity uncertainties as estimated by Kreemer et al. (2020) have median values of ∼0.1 mm/yr and ∼0.3 mm/yr respectively for the horizontal and vertical components (Figures S3a and S3b in Supporting Information S1). For the vertical gridded velocities, Kreemer et al. (2020) provided two different uncertainty estimation based on the comparison between gridded velocity values and, respectively, raw (hereafter "std1," Figure S3d in Supporting Information S1) or despeckled (hereafter "std2," Figure S3f in Supporting Information S1) GPS vertical velocities. std1 is up to 3 times larger than std2.

We consider three different three-dimensional (3D: horizontal and vertical) velocity data sets: (a) raw velocities at GPS sites and related uncertainties (hereafter "GPS-sites"; Figures 1c and 1d; Figures S3a, and S3b in Supporting Information S1); (b) gridded velocities with std1 vertical uncertainties (hereafter "gridded-std1"; Figures 1e and 1f; Figure S3d in Supporting Information S1); (c) gridded velocities with std2 vertical uncertainties (hereafter

"gridded-std2"; Figures 1e and 1f; Figure S3f in Supporting Information S1). In the last two cases we assumed a uniform value of 0.1 mm/yr for the uncertainties associated to the gridded horizontal velocities (Figures S3c and S3e in Supporting Information S1).

3. Methods

Nearly horizontal planar volcanic sources, such as sill-like magma intrusions, typically generate a single region of uplift at the surface and are inefficient at generating horizontal deformation (e.g., Segall, 2010; Troise et al., 2007). Pressurized sills-related deformation can be modeled using Tensile Rectangular Dislocations (TRDs) (Okada, 1985) with prescribed uniform opening embedded in a homogeneous elastic half-space (e.g., Delgado & Grandin, 2021; Jonsson, 2009). Here we employed the TRDs solutions of Nikkhoo et al. (2017). Each TRD is defined by its position, dimensions, orientation and opening. Since we are dealing with velocities, hereafter we refer to opening rates. In order to estimate the distribution of opening rates, we defined a grid of horizontal TRDs ("patches") with 30 km sides and oriented North-South. The patches dimension was chosen as a compromise between the horizontal spacing of GPS and gridded data points to reduce artifacts in the retrieved opening rate distribution (Amoruso et al., 2013). We fixed the overall extent of the TRDs grid to the study region size (400 km × 400 km). We first set its depth at 30 km (Moho) based on the seismic waves velocity anomaly (Section 1), and we additionally tested depths between 10 and 80 km.

For a given TRDs geometry, the velocities and opening rates are linearly related as

$$\mathbf{d} = \mathbf{Gm} + \boldsymbol{\epsilon} \tag{1}$$

where **d** is a $3N \times 1$ data-vector (N number of GPS sites/grid nodes) collecting the 3D observed velocity values, **m** is a $M \times 1$ model-vector (M number of TRD patches) collecting the distribution of opening rates, and $\boldsymbol{\epsilon}$ is a $3N \times 1$ vector containing observation uncertainties. **G** is a $3N \times M$ matrix expressing the effect of unitary opening rates and estimated assuming a homogeneous half-space with Poisson's ratio of 0.25. To avoid data over-fitting and nonphysical sharp spatial irregularities in the opening rates distribution, we applied a smoothing regularization via finite-difference approximation of the Laplacian operator (**L**). The smoothing amount to balance data-fit and opening rates-roughness is controlled through a regularization parameter k. The forward model therefore is

$$\begin{bmatrix} \mathbf{Wd} \\ \mathbf{0} \end{bmatrix} = \begin{bmatrix} \mathbf{WG} \\ k\mathbf{L} \end{bmatrix} \mathbf{m} \tag{2}$$

where **W** is a diagonal weighting matrix ($\mathbf{W}^T\mathbf{W} = \boldsymbol{\Sigma}^{-1}$, with $\boldsymbol{\Sigma}$ as data variance-covariance matrix). Furthermore, we imposed a positivity constraint on **m** to reproduce an inflation process (uplift). We solved the resulting weighted damped least-squares problem with inequality constraints using the non-negative least-squares (NNLS) iterative method by Lawson and Hanson (1995) (*lsqnonneg* Matlab function).

To select the optimal k, we tested both the *L*-curve (Hansen & O'Leary, 1993; Harris & Segall, 1987) and cross-validation (CV) (Hreinsdóttir et al., 2003; Matthews & Segall, 1993) methods and we finally used CV for the GPS-data case and *L*-curve for the gridded-data cases (Table 1; further details in Text S1 and Figure S4 in Supporting Information S1). Conversely, the positivity constraint precludes the use of the Akaike's Bayesian information criterion-based method (Fukuda & Johnson, 2008; Yabuki & Matsu'ura, 1992).

Since iterative NNLS methods do not construct an explicit expression for the model parameters **m**, hindering an explicit computation of related uncertainty (e.g., Menke, 2012), we employed the bootstrap method (Efron & Tibshirani, 1986) to estimate the opening rates uncertainty (Text S1 in Supporting Information S1).

As a further test on source parameters, we employed the horizontal penny-shaped crack model by Fialko et al. (2001) (using routines by Battaglia et al., 2013). We inverted for the depth, radius and dimensionless excess-pressure (pressure/shear modulus) rate of a source centered at ($X = 0$, $Y = 0$) through a non-linear Nelder-Mead optimization (Lagarias et al., 1998) testing different starting values for the inverted parameters.

We finally tested whether more isotropic sources (in an elastic half-space) could better explain the data using: (a) the quasi-analytical solutions for the pressurization of a single finite (triaxial) ellipsoidal cavity by Nikkhoo and Rivalta (2023); (b) the point compound dislocation model (point CDM) by Nikkhoo et al. (2017). The latter

Table 1
Inversion Results for TRDs and Penny-Shaped Crack Models

TRDs

GPS-sites

Depth[a] (km)	Smoothing factor (m*yr)	volume growth rate (m³/yr)	WRSS	RMSE (mm/yr)
10	8e12	4.899e7 ± 1.000e7	8705.909	0.5319
20	7e12	5.024e7 ± 1.165e7	8480.445	0.5316
30	6e12	4.976e7 ± 1.269e7	8396.177	0.5316
40	5e12	4.938e7 ± 1.395e7	8367.555	0.5322
50	5e12	4.883e7 ± 1.407e7	8398.961	0.5334
60	4e12	4.923e7 ± 1.582e7	8401.579	0.5343
80	3e12	5.053e7 ± 1.858e7	8452.646	0.5365

Gridded-std1

Depth[a] (km)	Smoothing factor (m*yr)	volume growth rate (m³/yr)	WRSS	RMSE (mm/yr)
10	1.5e13	4.513e7 ± 1.643e6	2668.756	0.1044
30	8e12	4.301e7 ± 1.946e6	2673.179	0.1094
60	4e12	4.079e7 ± 3.574e6	3200.680	0.1260
80	4e12	4.118e7 ± 3.934e6	3494.734	0.1351

Gridded-std2

Depth[a] (km)	Smoothing factor (m*yr)	volume growth rate (m³/yr)	WRSS	RMSE (mm/yr)
10	2e13	4.385e7 ± 2.010e6	11,838.209	0.0959
30	1.5e13	4.388e7 ± 2.096e6	13,396.295	0.0995
60	5e12	4.503e7 ± 4.961e6	17,216.117	0.1125
80	4e12	4.584e7 ± 6.924e6	20,829.661	0.1208

Penny-shaped crack

Data	Depth (km)	Radius (km)	Excess pressure-rate[b] (1/yr)	volume growth rate (m³/yr)	RMSE (mm/yr)
GPS-sites	48	173	7.9e−10	4.457e7	0.5351
Gridded-std1	27	176	1.5e−10	3.164e7	0.1210
Gridded-std2	23	224	4.1e−11	4.998e7	0.1233

[a]Fixed a priori. [b]Excess pressure is defined as pressure/shear modulus.

is composed of three mutually orthogonal rectangular dislocations representing planar and volumetric sources of various aspect ratios. We considered a horizontal grid of point CDMs located at the center of each TRD and at 30 km depth. We inverted for the source potency in three directions (ΔV_x, ΔV_y, ΔV_z) for each point CDM, using a weighted damped NNLS method analogous to the TRDs. A horizontal TRD-like model would correspond to a point CDM with only $\Delta V_z \neq 0$, whereas non-null values of ΔV_x and/or ΔV_y would indicate more equidimensional-like sources.

4. Results

TRDs inversion results suggest that the observed surface deformation would require the inflation of a sill-like source distributed over an area of up to $\sim 300 \times 300$ km^2 with total volume growth rate of about 0.045 km^3/yr (Table 1, Figure 2; Figure S5 in Supporting Information S1). The retrieved opening rate spatial distribution is mostly consistent across the three data sets reaching highest values (~ 0.8–1.3 mm/yr) at the center of RHM. In particular, for GPS-sites and gridded-std1 cases the highest opening rate is mostly concentrated slightly to the north-west of the Quaternary EVF activity location (Figures 2a.1 and 2b.1) and produces a horizontal velocity pattern mostly compatible with the area of significant dilatation rate (Kreemer et al., 2020) (Figures 2a.2 and 2b.2). In the gridded-std2 case, instead, the highest opening rate coincides with the Quaternary EVF activity location, where the highest uplift is observed (Figure 2c.1). This difference is mainly due to the overall higher uncertainty (lower weight) of vertical velocities for the GPS and gridded-std1 cases (Figures S3 and S5 in Supporting Information S1). The effect of the low signal-to-noise ratio of vertical data is also clear from solutions obtained imposing equal weights ($\mathbf{W} = \mathbf{I}$); the main features are still consistent with the "weighted" solutions (Figure S6 in Supporting Information S1). The estimated volume growth rates are consistent for the three data sets (~ 0.043–0.050 km^3/yr), with $\sim 13\%$ higher value in the GPS-data case. Due to the lower site coverage and higher data noise, opening rates uncertainty is higher for the GPS-data case (Figure S7 in Supporting Information S1), resulting in a higher volume growth rate uncertainty (0.01 km^3/yr, Table 1). The modeled deformation matches reasonably well with the observed one, with root-mean-square error RMSE ~ 0.5 mm/yr and 0.1 mm/yr respectively for GPS and gridded data sets (Figure 2). Further tests we conducted (adding rigid translation rates common to the whole data set; assuming a slight—up to 10°—dip angle; spatial filtering, removing horizontal outliers and/or vertical negative values in GPS data set) resulted in minor differences in the model parameters values.

We find a tendency to lower smoothing factors with higher TRDs depths (Table 1), since fewer patches with higher opening rates and covering a smaller area have a similar effect to smoother, spatially spread, opening rates distributions at shallower depths. Deeper sources result in slightly worse data fit, particularly for the gridded data sets (RMSE difference up to 20%). However, the misfit differences are not significant compared to data uncertainties and the results could be affected by some intrinsic level of subjectivity in the smoothing factor selection. The source depth is hard to constrain, but the volume growth rates at different depths are consistent with each other and within the uncertainty estimated for the 30 km depth solution.

Results for the horizontal penny-shaped crack are consistent with the TRDs model, with optimal source depth between 25 and 50 km and corresponding volume growth rates between 0.031 and 0.050 km^3/yr (Table 1).

Besides some inversion instabilities at the grid edges, the point CDM sources with gridded data result in low (<0.3) horizontal-to-vertical potency ratios (Figure S8 in Supporting Information S1) below the RHM. Results for GPS-sites data, even if still indicating higher ΔV_z values below the RHM, show a more complex pattern. The inversion is however quite sensitive to the low signal-to-noise ratio of the data. The total volume growth rate associated with the point CDM model (0.044–0.052 km^3/yr) is consistent with other tested models. The TRDs model is therefore suitable to reproduce the observed deformation and the threefold number of parameters involved in point CDMs is not needed.

Finally, the tests for different source shapes provide satisfying data-fit with sill-like source and consistent volume growth rate values, while excluding prolate spheroidals to explain the observed deformation.

5. Discussion and Conclusions

Our results indicate that, in the assumption of an elastic-half space, a subhorizontal magma body, or an aggregate of subhorizontal bodies, inflating at a total rate of up to 0.04 ± 0.01 km^3/yr, distributed over an area of up to
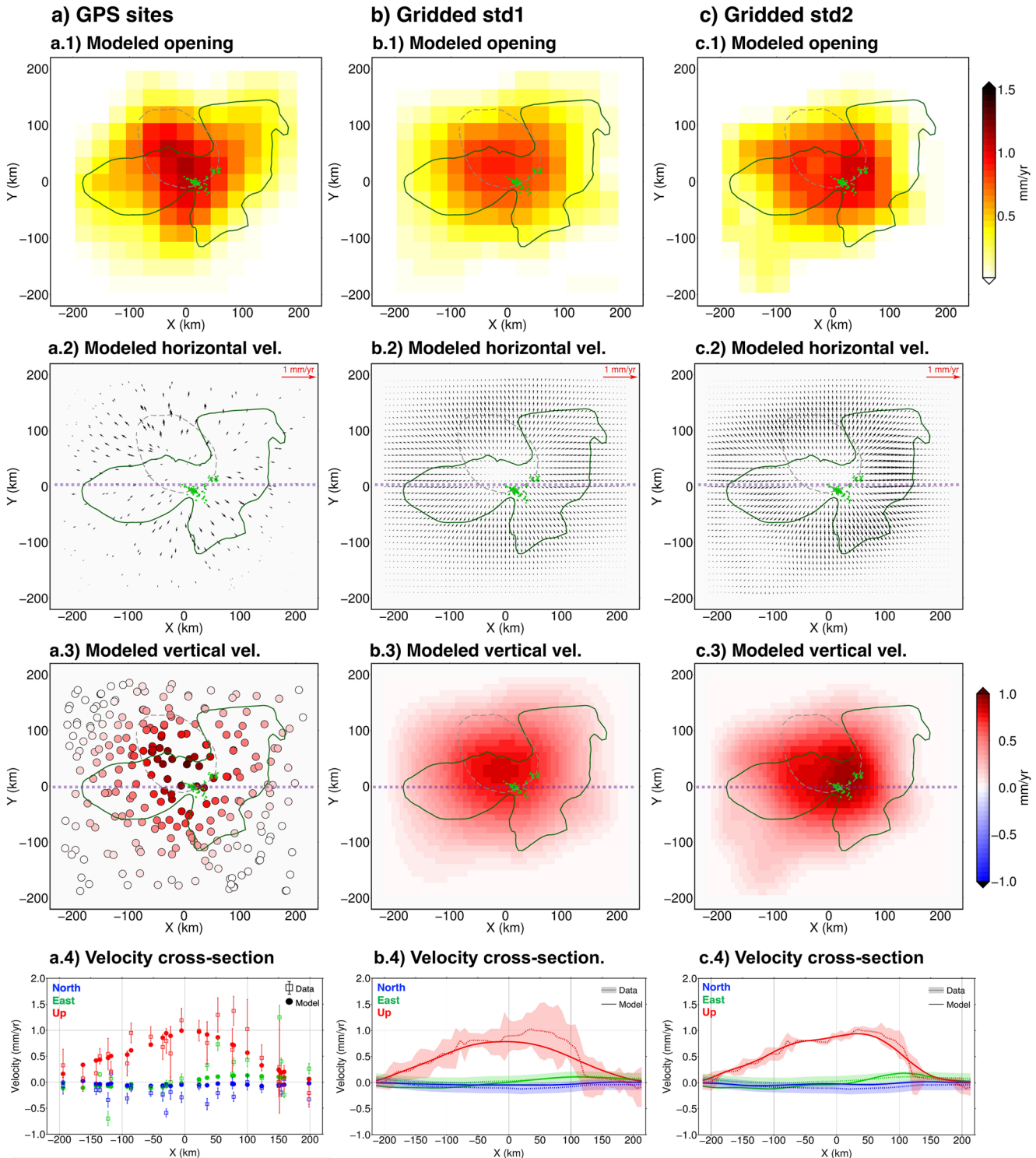
Figure 2. Model results for a TRDs grid at 30 km depth. The last row show modeled versus observed data cross-sections at $Y = 0$ km (dotted purple lines in maps). All other elements are the same as Figure 1.

300×300 km, and located at a poorly constrained depth between 20 and 60 km, would reproduce the deformation pattern observed at RHM (Figure 1b). Our model represents a first, simplified attempt at modeling the observed deformation at RHM with a magmatic intrusion mechanism. We discuss now the feasibility, limitations and possible interpretations of our results.

We considered a single source at different assigned depths, but ascending mantle melts may be trapped at various levels within the crust. A source shaped as an aggregate of subhorizontal, smaller magma lenses distributed over our preferred depth range would fit the deformation equally well (e.g., Amoruso & Crescentini, 2009). The presence of tabular zones of magma accumulation located at several depths, possibly forming a transcrustal magma system, has been suggested by recent seismicity, tomography, and petrological studies, multi-isotope gas analysis and magnetotelluric methods (e.g., Bräuer et al., 2013; Dahm et al., 2020; Hensch et al., 2019; Jödicke et al., 1983; Rizzo et al., 2021; Schmincke, 2007).

The involved large spatial extent and relatively shallow depths represent a challenge, as they put the source in the very-near field requiring finite-dimension source models at the limit of applicability of half-space analytical solutions (e.g., Fialko et al., 2001). Furthermore, within a linear-elastic framework, sills whose half-length is larger than their depth are unstable and tend to propagate away from their plane, due to the interaction with the free surface (Fialko, 2001). This would be the case if we interpreted our inferred source as a continuous magma body in an elastic half space.

Our estimated volume growth rate and source dimensions should be considered as upper values. Indeed, further complexities might play a non-negligible role and could decrease the estimated parameters values. The inferred size and growth rate for the sill, or aggregate of sub-horizontal melt lenses, is tied-to/trades-off-with the considered rheology. In purely elastic models all the surface deformation is generated by overpressure on the reservoir walls. At the examined depths (some tens of km) and time scales (at least 20 years, but possibly much longer), temperatures are elevated and prolonged magma accumulation may have further weakened the host rock, making elastic rheology unrealistic. Viscoelastic relaxation and/or thermal expansion would result in a broader surface uplift pattern which may account for part of the observed deformation (e.g., Lisowski et al., 2021; Newman et al., 2006; Novoa et al., 2019). Viscoelastic models can produce the same amplitude of displacement for significantly smaller pressure changes when compared to elastic solutions, and there is a gradual broadening of the uplift profile in layered viscoelastic models (e.g., Hickey & Gottsmann, 2014). Modeling a rheologically complex lithosphere for RHM is however challenging due to a lack of constraints on the recent deformation history. Even though the present-day uplift rate of ~1 mm/yr observed over the last ~20 years might be traceable back to several decades (e.g., Mälzer et al., 1983; Ziegler, 1992), uplift rates have varied considerably in geological times (Meyer & Stets, 2007).

Viscosity also affects the maximum depths at which sill-like intrusions could develop. Host rock viscosities 10 to 14 order of magnitudes higher than magma viscosity are required for tensile fracturing, and, thus, hydraulic fracturing to occur (Rubin, 1993). If deep (few tens of km) sills will be confirmed through, for example, imaging below Rhenish Massif, this could provide information on the host rocks rheology and the still poorly understood mechanisms of diking at lower crust/lithospheric mantle depths.

At the involved spatial scales (hundreds of km) earth curvature might also have some effect. In a spherical earth model there is less elastic material resisting deformation, requiring a smaller source to reproduce the observed deformation. Moreover, viscoelastic relaxation diffuses deformation away from the source and would further increase the importance of earth curvature (Segall, 2010).

Additional complexities such as topographic loading and material heterogeneities might also affect the estimated model parameters values.

We note that a combination of one or more sills with lower volume growth rate and a buoyant plume as proposed by Kreemer et al. (2020) could also reproduce the observed deformation. In our model, melt ascending from the mantle tends to collect in discrete magma pockets. Thus, magma emplacement becomes localized, inducing, or contributing to, lithosphere deformation (Figure 1b). Melt accumulation in the litosphere might be needed in the buoyant-body model by Kreemer et al. (2020), since it does not entirely reproduce the shape of the highest uplift area and it implies a buoyancy force distribution over a 150–180 km radius area, much larger than the imaged ~60 km diameter plume stem below RHM (Ritter, 2007; Ritter et al., 2001).

Our inferred deformation source could represent a volume of magma stagnation in the lithosphere over a large region beneath RHM, and could partly correspond to the wide layer of low seismic wave velocity inferred by Dahm et al. (2020) (Section 1). Magma might originate from the rise of a mantle plume underneath or decompression-induced melting from passive rifting (e.g., Acocella, 2021). Melt ponding in subhorizontal fractures in the elastic lithosphere (underplating) has been documented in other regions to explain long-term uplift

rates and surface deformation (Pedraza De Marchi et al., 2021; Thybo & Artemieva, 2013). Active magmatic underplating has been hypothesized for the region beneath the Eger rift and Cheb basin (Hrubcová et al., 2017), and for the Limagne graben (Michon & Merle, 2001), which are thought to have a common rift formation mechanism to the EVF.

The inferred dimensions for our source are rather unprecedented, and probably overestimated, as previously discussed. Nevertheless, there are evidences of large extinct/active magma bodies (10^2–10^3 km radius; e.g., Thybo & Artemieva, 2013; Cruden et al., 2018; Acocella, 2021). A large mid-crustal sill ($\sim$250 × 100 km) and an even larger partial-melt layer at the Moho lay beneath Snake River Plain, USA (Peng & Humphreys, 1998). The Altiplano Puna Magma Body in Central Andes, located at 14–20 km depth, has a sill-like geometry with $\sim$200 km diameter and is associated with an ongoing uplift of $\sim$10 mm/year concentrated in a smaller area (Perkins et al., 2016). Other large, deep (30–40 km) magma bodies exist, but they are often imaged through 2D tomography sections, so their full size is unconstrained (Thybo & Artemieva, 2013).

The upper-end value of volume growth rate we inferred ($\sim$$10^{-2}$ km^3/yr) is considerably higher than prior estimates of magma extraction rate for EVF. These are however mostly based on erupted material at local scales (e.g., lower-crust intrusion rates of 10^{-3}—10^{-4} km^3/yr beneath the East EVF; Dahm et al., 2020). Estimates of carbon dioxide fluxes from the whole Eifel region are in the order of 0.5–1 Mt/yr (Puchelt, 1983). Assuming a magma density of 2600 kg/m^3, our volume growth rate corresponds to a mass accumulation rate of $1.2 \cdot 10^{11}$ kg/yr. This means that the CO_2 fluxes would correspond to about 1% of the magma mass rate. Similar ratios of CO_2 in parental magmas are found in continental rift regions (Aiuppa et al., 2021).

Possible implications for magma propagation and future eruptions based on our volume growth rate can be inferred from Galetto et al. (2022), who found that magma volume increase in crustal reservoirs at rates <0.01 km^3/yr have not led to magma propagation in 90% of cases. The magma supply episodes analyzed by Galetto et al. (2022) were located in the middle-to-upper crust, so in the RHM case the eruption likelihood would be lower, but still deserves attention, as magma may ascend relatively swiftly from large depths (e.g., Mayotte and Cumbre Vieja, La Palma, eruptions; Cesca et al., 2020; del Fresno et al., 2023).

Even if previous studies showed no significant gravity anomaly unequivocally related to the EVF plume or to the regional uplift (Ritter et al., 2007; Van Camp et al., 2011), accurate gravity measurements could in principle constrain the total mass and the density of the potentially intruding material (e.g., Nikkhoo & Rivalta, 2022). The expected free-air corrected gravity changes at the surface associated with our TRDs model is <0.2 μGal/yr (Text S2 in Supporting Information S1), showing that gravity changes above measure uncertainties would require long observation periods. However, absolute gravimeters campaigns of sub-μGal accuracy, if carried out over protracted time periods, may help measuring the uplift with higher accuracy, after removing the effects from other deformation sources such as hydrological and anthropic activity (Nikkhoo & Rivalta, 2022; Van Camp et al., 2011).

In conclusion, understanding the process causing the current RHM uplift and the recent unrest at EVF requires further studies and new and complementary observations at multiple spatial and temporal scales (e.g., deformation, seismicity, tomography, geochemistry). The spatial extent of the area under examination and the low deformation magnitude represent a challenge. GPS data were fundamental in revealing the ongoing deformation, but better constraint of the deformation source would require longer, more accurate (particularly of the horizontal-to-vertical ratio), and possibly spatially denser measurements, together with further understanding of other ongoing processes at large (e.g., GIA), regional (e.g., faulting and seismicity within the Lower Rhine Graben) and local (e.g., human activity) scales. Currently ongoing measuring campaigns (e.g., dense seismic networks) at EVF may shed new light on the underlying magmatic system and its implications.

Data Availability Statement

The final GPS and gridded velocities and GPS time-series can be found in the Supporting Information of Kreemer et al. (2020) and in Kreemer (2020), while the original GPS time-series can be retrieved from Blewitt et al. (2018). Gridded data uncertainties were provided by Corné Kreemer. We used routines by Battaglia et al. (2013), Nikkhoo et al. (2017), Beauducel (2022), and Nikkhoo and Rivalta (2023). Data and main codes are collected in Silverii et al. (2023).

References

Acocella, V. (2021). *Volcano-tectonic processes*. Springer International Publishing. Retrieved from https://books.google.it/books?id=T9EtEAAAQBAJ

Aiuppa, A., Casetta, F., Coltorti, M., Stagno, V., & Tamburello, G. (2021). Carbon concentration increases with depth of melting in Earth's upper mantle. *Nature Geoscience*, *14*(9), 697–703. https://doi.org/10.1038/s41561-021-00797-y

Amoruso, A., Barba, S., Crescentini, L., & Megna, A. (2013). Inversion of synthetic geodetic data for dip-slip faults: Clues to the effects of lateral heterogeneities and data distribution in geological environments typical of the Apennines (Italy). *Geophysical Journal International*, *192*(2), 745–758. https://doi.org/10.1093/gji/ggs042

Amoruso, A., & Crescentini, L. (2009). Shape and volume change of pressurized ellipsoidal cavities from deformation and seismic data. *Journal of Geophysical Research*, *114*(B2), B02210. https://doi.org/10.1029/2008JB005946

Artemieva, I. M. (2019). Lithosphere structure in europe from thermal isostasy. *Earth-Science Reviews*, *188*, 454–468. https://doi.org/10.1016/j.earscirev.2018.11.004

Battaglia, M., Cervelli, P. F., & Murray, J. R. (2013). dMODELS: A MATLAB software package for modeling crustal deformation near active faults and volcanic centers [Software]. Journal of Volcanology and Geothermal Research, *254*, 1–4. https://doi.org/10.1016/j.jvolgeores.2012.12.018

Beauducel, F. (2022). OKUBO: Gravity change due to shear and tensile faults [Software]. MATLAB Central File Exchange. Retrieved from https://www.mathworks.com/matlabcentral/fileexchange/37158-okubo-gravity-change-due-to-shear-and-tensile-faults

Blewitt, G., Hammond, W., & Kreemer, C. (2018). Harnessing the GPS data explosion for interdisciplinary science [Dataset]. Eos, *99*. https://doi.org/10.1029/2018EO104623

Bräuer, K., Kämpf, H., Niedermann, S., & Strauch, G. (2013). Indications for the existence of different magmatic reservoirs beneath the Eifel area (Germany): A multi-isotope (C, N, He, Ne, Ar) approach. *Chemical Geology*, *356*, 193–208. https://doi.org/10.1016/j.chemgeo.2013.08.013

Caracausi, A., Avice, G., Burnard, P. G., Füri, E., & Marty, B. (2016). Chondritic xenon in the Earth's mantle. *Nature*, *533*(7601), 82–85. https://doi.org/10.1038/nature17434

Cesca, S., Letort, J., Razafindrakoto, H. N. T., Heimann, S., Rivalta, E., Isken, M. P., et al. (2020). Drainage of a deep magma reservoir near Mayotte inferred from seismicity and deformation. *Nature Geoscience*, *13*(1), 87–93. https://doi.org/10.1038/s41561-019-0505-5

Cruden, A. R., McCaffrey, K. J. W., & Bunger, A. P. (2018). Geometric scaling of tabular igneous intrusions: Implications for emplacement and growth. In C. Breitkreuz & S. Rocchi (Eds.), *Physical geology of shallow magmatic systems: Dykes, sills and laccoliths* (pp. 11–38). Springer International Publishing. https://doi.org/10.1007/11157_2017_1000

Dahm, T., Stiller, M., Mechie, J., Heimann, S., Hensch, M., Woith, H., et al. (2020). Seismological and geophysical signatures of the deep crustal magma systems of the Cenozoic volcanic fields beneath the Eifel, Germany. *Geochemistry, Geophysics, Geosystems*, *21*(9), e2020GC009062. https://doi.org/10.1029/2020GC009062

del Fresno, C., Cesca, S., Klügel, A., Domínguez Cerdeña, I., Díaz-Suárez, E. A., Dahm, T., et al. (2023). Magmatic plumbing and dynamic evolution of the 2021 La Palma eruption. *Nature Communications*, *14*(1), 358. https://doi.org/10.1038/s41467-023-35953-y

Delgado, F., & Grandin, R. (2021). Dynamics of episodic magma Injection and migration at Yellowstone caldera: Revisiting the 2004–2009 episode of caldera uplift with InSAR and GPS data. *Journal of Geophysical Research: Solid Earth*, *126*(8), e2021JB022341. https://doi.org/10.1029/2021JB022341

Demoulin, A., & Hallot, E. (2009). Shape and amount of the Quaternary uplift of the western Rhenish shield and the Ardennes (western Europe). *Tectonophysics*, *474*(3), 696–708. https://doi.org/10.1016/j.tecto.2009.05.015

Efron, B., & Tibshirani, R. (1986). Bootstrap methods for standard errors, confidence intervals, and other measures of statistical accuracy. *Statistical Science*, *1*(1), 54–75. https://doi.org/10.1214/ss/1177013815

Fekiacova, Z., Mertz, D. F., & Renne, P. R. (2007). Geodynamic setting of the tertiary Hocheifel volcanism (Germany), Part I: 40Ar/39Ar geochronology. In J. R. R. Ritter & U. R. Christensen (Eds.), *Mantle plumes: A multidisciplinary approach* (pp. 207–240). Springer Berlin Heidelberg. https://doi.org/10.1007/978-3-540-68046-8_6

Fialko, Y. (2001). On origin of near-axis volcanism and faulting at fast spreading mid-ocean ridges. *Earth and Planetary Science Letters*, *190*(1), 31–39. https://doi.org/10.1016/S0012-821X(01)00376-4

Fialko, Y., Khazan, Y., & Simons, M. (2001). Deformation due to a pressurized horizontal circular crack in an elastic half-space, with applications to volcano geodesy. *Geophysical Journal International*, *146*(1), 181–190. https://doi.org/10.1046/j.1365-246X.2001.00452.x

Förster, M. W., Zemlitskaya, A., Otter, L. M., Buhre, S., & Sirocko, F. (2020). Late Pleistocene Eifel eruptions: Insights from clinopyroxene and glass geochemistry of tephra layers from Eifel laminated sediment Archive sediment cores. *Journal of Quaternary Science*, *35*(1–2), 186–198. https://doi.org/10.1002/jqs.3134

Fukuda, J., & Johnson, K. M. (2008). A fully Bayesian inversion for spatial distribution of fault slip with objective smoothing. *Bulletin of the Seismological Society of America*, *98*(3), 1128–1146. https://doi.org/10.1785/0120070194

Galetto, F., Acocella, V., Hooper, A., & Bagnardi, M. (2022). Eruption at basaltic calderas forecast by magma flow rate. *Nature Geoscience*, *15*(7), 580–584. https://doi.org/10.1038/s41561-022-00960-z

Hansen, P. C., & O'Leary, D. P. (1993). The use of the L-curve in the regularization of discrete Ill-posed problems. *SIAM Journal on Scientific Computing*, *14*(6), 1487–1503. https://doi.org/10.1137/0914086

Harris, R. A., & Segall, P. (1987). Detection of a locked zone at depth on the Parkfield, California, segment of the San Andreas Fault. *Journal of Geophysical Research*, *92*(B8), 7945–7962. https://doi.org/10.1029/JB092iB08p07945

Henrion, E., Masson, F., Doubre, C., Ulrich, P., & Meghraoui, M. (2020). Present-day deformation in the upper Rhine graben from GNSS data. *Geophysical Journal International*, *223*(1), 599–611. https://doi.org/10.1093/gji/ggaa320

Hensch, M., Dahm, T., Ritter, J., Heimann, S., Schmidt, B., Stange, S., & Lehmann, K. (2019). Deep low-frequency earthquakes reveal ongoing magmatic recharge beneath Laacher See Volcano (Eifel, Germany). *Geophysical Journal International*, *216*(3), 2025–2036. https://doi.org/10.1093/gji/ggy532

Hickey, J., & Gottsmann, J. (2014). Benchmarking and developing numerical Finite Element models of volcanic deformation. *Journal of Volcanology and Geothermal Research*, *280*, 126–130. https://doi.org/10.1016/j.jvolgeores.2014.05.011

Hreinsdóttir, S., Freymueller, J. T., Fletcher, H. J., Larsen, C. F., & Bürgmann, R. (2003). Coseismic slip distribution of the 2002 MW7.9 Denali fault earthquake, Alaska, determined from GPS measurements. *Geophysical Research Letters*, *30*(13), 1670. https://doi.org/10.1029/2003GL017447

Hrubcová, P., Geissler, W. H., Bräuer, K., Vavryčuk, V., Tomek, V., & Kämpf, H. (2017). Active magmatic underplating in western Eger rift, central Europe. *Tectonics*, *36*(12), 2846–2862. https://doi.org/10.1002/2017TC004710

Husson, L., Bodin, T., Spada, G., Choblet, G., & Kreemer, C. (2018). Bayesian surface reconstruction of geodetic uplift rates: Mapping the global fingerprint of glacial isostatic adjustment. *Journal of Geodynamics*, *122*, 25–40. https://doi.org/10.1016/j.jog.2018.10.002

Jödicke, H., Untiedt, J., Olgemann, W., Schulte, L., & Wagenitz, V. (1983). Electrical conductivity structure of the crust and upper mantle beneath the Rhinish massif. In K. Fuchs, K. von Gehlen, H. Mälzer, H. Murawski, & A. Semmel (Eds.), *Plateau uplift* (pp. 288–302). Springer Berlin Heidelberg.

Jonsson, S. (2009). Stress interaction between magma accumulation and trapdoor faulting on sierra Negra volcano, Galapagos. *Tectonophysics*, *471*(1), 36–44. https://doi.org/10.1016/j.tecto.2008.08.005

Jung, S., Pfänder, J. A., Brügmann, G., & Stracke, A. (2005). Sources of primitive alkaline volcanic rocks from the Central European Volcanic Province (Rhön, Germany) inferred from Hf, Os and Pb isotopes. *Contributions to Mineralogy and Petrology*, *150*(5), 546–559. https://doi.org/10.1007/s00410-005-0029-4

Kreemer, C. (2020). Replication data for: Geodetic evidence for a buoyant mantle plume beneath the Eifel volcanic area, NW Europe [Dataset]. Harvard Dataverse. https://doi.org/10.7910/DVN/ONATFP

Kreemer, C., Blewitt, G., & Davis, P. M. (2020). Geodetic evidence for a buoyant mantle plume beneath the Eifel volcanic area, NW Europe [Dataset]. Geophysical Journal International, *222*, 1316–1332. https://doi.org/10.1093/gji/ggaa227

Lagarias, J. C., Reeds, J. A., Wright, M. H., & Wright, P. E. (1998). Convergence properties of the Nelder–Mead simplex method in low dimensions. *SIAM Journal on Optimization*, *9*(1), 112–147. https://doi.org/10.1137/S1052623496303470

Lawson, C. L., & Hanson, R. J. (1995). *Solving least squares problems* (Vol. 15). Society for Industrial and Applied Mathematics (SIAM). (Revised reprint of the 1974 original).

Lisowski, M., McCaffrey, R., Wicks, C. W., & Dzurisin, D. (2021). Geodetic Constraints on a 25-year magmatic inflation episode near Three Sisters, central Oregon. *Journal of Geophysical Research: Solid Earth*, *126*(12), e2021JB022360. https://doi.org/10.1029/2021JB022360

Lustrino, M., & Carminati, E. (2007). Phantom plumes in Europe and the circum-Mediterranean region. In *Plates, plumes and planetary processes*. Geological Society of America. https://doi.org/10.1130/2007.2430(33)

Mälzer, H., Hein, G., & Zippelt, K. (1983). Height changes in the Rhinish massif: Determination and analysis. In K. Fuchs, K. von Gehlen, H. Mälzer, H. Murawski, & A. Semmel (Eds.), *Plateau uplift* (pp. 164–176). Springer Berlin Heidelberg.

Matthews, M., & Segall, P. (1993). Estimation of depth-dependent fault slip from measured surface deformation with application to the 1906 San Francisco Earthquake. *Journal of Geophysical Research*, *98*(B7), 12153–12163. https://doi.org/10.1029/93JB00440

Mechie, J., Prodehl, C., & Fuchs, K. (1983). The long-range seismic refraction experiment in the Rhenish Massif. In K. Fuchs, K. von Gehlen, H. Mälzer, H. Murawski, & A. Semmel (Eds.), *Plateau uplift*. Springer. https://doi.org/10.1007/978-3-642-69219-2_31

Menke, W. (2012). *Geophysical data analysis: Discrete inverse theory* (3rd ed.). Academic Press. https://doi.org/10.1016/C2011-0-69765-0

Meyer, W., & Stets, J. (2007). Quaternary uplift in the eifel area. In J. R. R. Ritter & U. R. Christensen (Eds.), *Mantle plumes: A multidisciplinary approach* (pp. 369–378). : Springer Berlin Heidelberg. https://doi.org/10.1007/978-3-540-68046-8_11

Michon, L., & Merle, O. (2001). The evolution of the Massif Central Rift; spatio-temporal distribution of the volcanism. *Bulletin de la Societe Geologique de France*, *172*(2), 201–211. https://doi.org/10.2113/172.2.201

Newman, A. V., Dixon, T. H., & Gourmelen, N. (2006). A four-dimensional viscoelastic deformation model for Long Valley Caldera, California, between 1995 and 2000. *Journal of Volcanology and Geothermal Research*, *150*(1–3), 244–269. https://doi.org/10.1016/j.jvolgeores.2005.07.017

Nikkhoo, M., & Rivalta, E. (2022). Analytical solutions for gravity changes caused by triaxial volumetric sources. *Geophysical Research Letters*, *49*(8), e2021GL095442. https://doi.org/10.1029/2021GL095442

Nikkhoo, M., & Rivalta, E. (2023). Surface deformations and gravity changes caused by pressurized finite ellipsoidal cavities [Software]. *Geophysical Journal International*, *232*(1), 643–655. https://doi.org/10.1093/gji/ggac351

Nikkhoo, M., Walter, T. R., Lundgren, P. R., & Prats-Iraola, P. (2017). Compound dislocation models (CDMs) for volcano deformation analyses [Software]. Geophysical Journal International, *208*, 877–894. https://doi.org/10.1093/gji/ggw427

Novoa, C., Remy, D., Gerbault, M., Baez, J., Tassara, A., Cordova, L., et al. (2019). Viscoelastic relaxation: A mechanism to explain the decennial large surface displacements at the Laguna del Maule silicic volcanic complex. *Earth and Planetary Science Letters*, *521*, 46–59. https://doi.org/10.1016/j.epsl.2019.06.005

Nowell, D. A. G., Jones, M. C., & Pyle, D. M. (2006). Episodic quaternary volcanism in France and Germany. *Journal of Quaternary Science*, *21*(6), 645–675. https://doi.org/10.1002/jqs.1005

Okada, Y. (1985). Surface deformation due to shear and tensile faults in a half-space. *Bulletin of the Seismological Society of America*, *75*(4), 1135–1154. https://doi.org/10.1785/bssa0750041135

Pedraza De Marchi, A. C., Ghidella, M. E., Tocho, C. N., & Franzese, J. R. (2021). Flexural uplift and magmatic underplating anomaly on the argentine continental margin: Profile at 43.5°s. *Marine Geophysical Researches*, *42*(2), 16. https://doi.org/10.1007/s11001-021-09437-x

Peng, X., & Humphreys, E. D. (1998). Crustal velocity structure across the eastern Snake River plain and the Yellowstone swell. *Journal of Geophysical Research*, *103*(B4), 7171–7186. https://doi.org/10.1029/97JB03615

Perkins, J. P., Ward, K. M., de Silva, S. L., Zandt, G., Beck, S. L., & Finnegan, N. J. (2016). Surface uplift in the central Andes driven by growth of the Altiplano Puna magma body. *Nature Communications*, *7*(1), 13185. https://doi.org/10.1038/ncomms13185

Prodehl, C., Mueller, S., & Haak, V. (2006). Chapter 4 the European Cenozoic rift system. In K. Olsen (Ed.), *Continental rifts: Evolution, structure, tectonics* (Vol. 25, pp. 133–212). Elsevier. https://doi.org/10.1016/S0419-0254(06)80012-1

Puchelt, H. (1983). Carbon dioxide in the Rhinish massif. In K. Fuchs, K. von Gehlen, H. Mälzer, H. Murawski, & A. Semmel (Eds.), *Plateau uplift* (p. 152). Springer Berlin Heidelberg.

Regenauer-Lieb, K. (1998). Dilatant plasticity applied to Alpine collision: Ductile void growth in the intraplate area beneath the Eifel volcanic field. *Journal of Geodynamics*, *27*(1), 1–21. https://doi.org/10.1016/S0264-3707(97)00024-0

Reinig, F., Wacker, L., Jöris, O., Oppenheimer, C., Guidobaldi, G., Nievergelt, D., et al. (2021). Precise date for the Laacher see eruption synchronizes the Younger Dryas. *Nature*, *595*(7865), 66–69. https://doi.org/10.1038/s41586-021-03608-x

Ritter, J. R. R. (2007). The seismic signature of the Eifel plume. In J. R. R. Ritter & U. R. Christensen (Eds.), *Mantle plumes: A multidisciplinary approach* (pp. 379–404). Springer Berlin Heidelberg. https://doi.org/10.1007/978-3-540-68046-8_12

Ritter, J. R. R., Jordan, M., Christensen, U. R., & Achaue, U. (2001). A mantle plume below the Eifel volcanic fields, Germany. *Earth and Planetary Science Letters*, *186*(1), 7–14. https://doi.org/10.1016/S0012-821X(01)00226-6

Ritter, J. R. R., Mathar, J. P., Jordan, M., & Gabriel, G. (2007). Gravity observations in the western Rhinish massif and forward modelling of the Eifel plume bouguer anomaly. In J. R. R. Ritter & U. R. Christensen (Eds.), *Mantle plumes: A multidisciplinary approach* (pp. 465–476). Springer Berlin Heidelberg. https://doi.org/10.1007/978-3-540-68046-8_16

Rizzo, A. L., Faccini, B., Casetta, F., Faccincani, L., Ntaflos, T., Italiano, F., & Coltorti, M. (2021). Melting and metasomatism in West Eifel and Siebengebirge Sub-Continental Lithospheric Mantle: Evidence from concentrations of volatiles in fluid inclusions and petrology of ultramafic xenoliths. *Chemical Geology*, *581*, 120400. https://doi.org/10.1016/j.chemgeo.2021.120400

Rubin, A. M. (1993). Tensile fracture of rock at high confining pressure: Implications for dike propagation. *Journal of Geophysical Research*, *98*(B9), 15919–15935. https://doi.org/10.1029/93JB01391

Schmincke, H.-U. (2007). The quaternary volcanic fields of the east and west Eifel (Germany). In J. R. R. Ritter & U. R. Christensen (Eds.), *Mantle plumes: A multidisciplinary approach* (pp. 241–322). Springer Berlin Heidelberg. https://doi.org/10.1007/978-3-540-68046-8_8

Segall, P. (2010). *Earthquake and volcano deformation* (Vol. 15). Princeton University Press. https://doi.org/10.1515/9781400833856

Silverii, F., Mantiloni, L., Rivalta, E., & Dahm, T. (2023). Codes and data for the submitted manuscript Lithospheric sill intrusions and present-day ground deformation at Rhenish Massif, Central Europe [Software]. Zenodo. https://doi.org/10.5281/zenodo.8406604

Thybo, H., & Artemieva, I. (2013). Moho and magmatic underplating in continental lithosphere. *Tectonophysics*, *609*, 605–619. https://doi.org/10.1016/j.tecto.2013.05.032

Troise, C., De Natale, G., Pingue, F., Obrizzo, F., De Martino, P., Tammaro, U., & Boschi, E. (2007). Renewed ground uplift at Campi Flegrei caldera (Italy): New insight on magmatic processes and forecast. *Geophysical Research Letters*, *34*(3), L03301. https://doi.org/10.1029/2006GL028545

Van Camp, M., de Viron, O., Scherneck, H.-G., Hinzen, K.-G., Williams, S. D. P., Lecocq, T., et al. (2011). Repeated absolute gravity measurements for monitoring slow intraplate vertical deformation in western Europe. *Journal of Geophysical Research*, *116*(B8), B08402. https://doi.org/10.1029/2010JB008174

Walker, K. T., Bokelmann, G. H. R., Klemperer, S. L., Bock, G., & The Eifel Plume Team. (2007). Seismic anisotropy in the asthenosphere beneath the Eifel region, western Germany. In J. R. R. Ritter & U. R. Christensen (Eds.), *Mantle plumes*. Springer. https://doi.org/10.1007/978-3-540-68046-8_15

Wessel, P., Smith, W. H., Scharroo, R., Luis, J., & Wobbe, F. (2013). Generic mapping tools: Improved version released. *Eos, Transactions American Geophysical Union*, *94*(45), 409–410. https://doi.org/10.1002/2013EO450001

Wilson, M., & Downes, H. (1992). Mafic alkaline magmatism associated with the European Cenozoic rift system. *Tectonophysics*, *208*(1), 173–182. https://doi.org/10.1016/0040-1951(92)90343-5

Yabuki, T., & Matsu'ura, M. (1992). Geodetic data inversion using a Bayesian information criterion for spatial distribution of fault slip. *Geophysical Journal International*, *109*(2), 363–375. https://doi.org/10.1111/j.1365-246X.1992.tb00102.x

Ziegler, P. A. (1992). European Cenozoic rift system. *Tectonophysics*, *208*(1), 91–111. https://doi.org/10.1016/0040-1951(92)90338-7